Quantum regime of a two-dimensional phonon cavity

Aleksey N. Bolgar,[1,*] Julia I. Zotova,[1] Daniil D. Kirichenko,[1] Ilia S. Besedin,[2]
Aleksander V. Semenov,[1,3] Rais S. Shaikhaidarov,[1,4] and Oleg V. Astafiev[1,5,6,†]

[1]*Moscow Institute of Physics and Technology, Institutskiy per. 9, Dolgoprudny, Russia*
[2]*National University for Science and Technology (MISiS), Leninskiy pr. 4, Moscow 119049, Russia*
[3]*Moscow State Pedagogical University, Malaya Pirogovskaya str. 1/1, Moscow 119435, Russia*
[4]*Royal Holloway University of London, Egham Surrey TW20 0EX, United Kingdom*
[5]*Royal Holloway, University of London, Egham Surrey TW20 0EX, United Kingdom*
[6]*National Physical Laboratory, Teddington, TW11 0LW, United Kingdom*

We realize the quantum regime of a surface acoustic wave (SAW) resonator by demonstrating vacuum Rabi mode splitting due to interaction with a superconducting artificial atom. Reaching the quantum regime is physically difficult and technologically challenging since SAW devices consist of large arrays of narrow metal strips. This work paves the way for realizing analogues of quantum optical phenomena with phonons and can be useful in an on-chip quantum electronics.

Quantum Acoustodynamics (QAD) is a new direction of quantum mechanics studying interaction of acoustic waves and phonons with quantum systems [1–6] and particularly with artificial ones [7–9]. Recently quantum acoustics has been focused on establishing the quantum regime in phonon systems [10–13]. The coupling to the vacuum mechanical mode of bulk acoustic resonators has been demonstrated in Ref. [1, 14]. Although, this was an important achievement, such an approach is more difficult for integration in two dimensional circuits because of issues in implementation of the bulk resonators in comparison with planar systems, since bulk resonators fabrication often require many layers of litoghaphy [1] or use the substrate as a medium for the resonator [14]. As it has been recently demonstrated in Ref. [3], these problems can be solved by utilizing surface acoustic waves (SAWs). Most recent research has already demonstrated an interaction between the qubit and a SAW resonator [2, 15], however the quantum regime was not fully reached. To reach the quantum regime in a SAW cavity, a series of physical and technological challenges must be overcome. Particularly, to exceed thermal fluctuations in dilution refrigerators by phonon energies, the acoustic frequencies must lie in the gigahertz range, which corresponds to submicron wavelengths opposite to commercially used SAW devices operating in megahertz or lower frequency ranges. Another problem is a lack of optical like mirrors (such as thin film mirrors with high reflectivity), which is solved by fabricating Bragg type gratings with a large number of nanometer metallic stripes. This requires development of advanced nanotechnology methods.

In this work, we successfully realize the quantum regime of a two-dimensional SAW cavity, demonstrated via a vacuum Rabi splitting with a vacuum cavity mode. The studied system is an artificial atom coupled to the cavity on a quartz crystal. Further development will result in a realization of series of analogues of different quantum optical effects in two dimensions and can help create compact elements for quantum informatics, particularly in hybrid devices combining advantages of optical and superconducting quantum technologies [16].

Surface acoustic waves in piezoelectrics were used for a long time in compact electronic elements operating in a megahertz range such as RF filters, resonators, delay lines etc. [17–21]. One of the main advantages of planar SAW devices is their small size determined by a slow speed of sound compared to electromagnetic waves and therefore up to five orders of magnitude shorter wavelengths for the same frequencies. It has been recently shown that superconducting artificial atoms, successfully exploited for coherent control of photons [22] and demonstration of quantum optics with single quantum systems [23], can also be used for control of single phonons and more generally for quantum acoustodynamics [2, 3, 24]. The next important milestone must be the demonstration of the interaction of the artificial atom with quantised resonator modes.

To describe our SAW resonator interacting with the artificial atom we use optical Jaynes-Cummings model, usually describing an atom in an optical resonator, substituting the photon creation (annihilation) operators by phonon ones $b^\dagger(b)$. With this substitution the Hamiltonian reads [25]

$$H = \frac{\hbar\omega_a}{2}\sigma_z + \hbar\omega_r b^\dagger b + \hbar g(b^\dagger\sigma^- + b\sigma^+), \qquad (1)$$

where σ_z is the Pauli matrix, $\sigma^+(\sigma^-)$ is the creation (annihilation) operator of the two-level system excited state. The first term represents the two-level atom with energy splitting $\hbar\omega_a$, the second one describes the SAW resonator with resonant frequency ω_r and the third is the resonator-atom interaction with coupling strength $\hbar g$.

Our device, shown in Fig. 1, is fabricated on a quartz substrate. It consists of an acoustic resonator with a superconducting artificial atom inside. The resonator is a 2D Fabry-Perot cavity, formed by two Bragg gratings [26, 27]. To excite and to detect the SAWs we add two identical interdigital transducer ports (IDTs) inside the resonator. The IDT converts applied ac-voltage into an

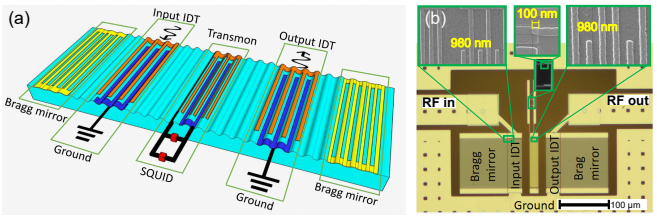

FIG. 1. The device. (a) A schematic 3D representation of the sample. Two identical IDT ports and the transmon qubit are located inside the SAW cavity. The SAW resonator is formed by two Bragg gratings, consisting of 200 periodic stripe electrodes each, with a period p, where $p = 980$ nm. Distance between the gratings is $225 \times p/2 = 110.7$ μm. IDT ports consist of 29 periodic identical cells with a period p. Each cell consists of 2 electrodes, connected to bars at opposite sides. The distance between the IDT port and the adjacent grating is $d_1 = (1 + 1/8)p$. The transmon qubit is located between the IDT ports and contains a SQUID shunted by an IDT capacitance. The qubit IDT has 18 cells. Each cell consists of 3 electrodes per period p, which minimizes its mechanical reflection of acoustic waves, in order to suppress parasitic resonances this element would otherwise cause [17]. The length of all electrodes in our device is $W = 100$ μm. The width of the electrodes of the gratings and IDT ports is $p/4$, and the width of the qubit IDT electrodes is $p/6$. (b) Optical micrographs of the sample with insets showing zoomed stripe structures and a Josephson junction, obtained with a scanning electron microscope (SEM).

acoustic wave and it is formed by a periodic array of alternating electrodes with a fixed pattern per period. We use two distinct IDT patterns with 2 and 3 electrodes per period, as shown in Fig. 1.

A tuneable two-level artificial atom consists of a SQUID shunted by an IDT structure, playing the role of both a qubit capacitance and a coupler to SAWs in the resonator. The qubit IDT has the same period as IDT ports and mirrors and its electrodes are positioned at the expected antinodes of standing acoustic wave in the resonator.

The device is fabricated in two steps of electron beam lithography and one step of optic laser lithography. Firstly, we form coplanar lines and ground planes using optic lithography. Then we fabricate IDTs and gratings and finally the SQUID, using the standard two-angle shadow evaporation technique. The most challenging process is the lithography of the gratings and IDTs, as their stripes are as narrow as 170 nm, while their length is 100 μm (the aspect ratio is about 600) and the total number of stripes is close to a thousand. All structures are made of Al and the metallic stripes are formed by deposition of the metal through a mask of organic resist with Al capping. Al capping is created after the mask is developed by evaporating 30 nm of Al at large angles to the surface normal, so that it creates an additional undercut. To succeed in fabricating the stripes many try-and-error attempts for adjusting the fabrication parameters have been made.

Connection of the aluminum layers is provided via large capacitances, formed by an oxide between large aluminum pads. Since, according to our calculations, these capacitances are more than 200 times larger than capacitance of the transmon qubit itself, they provide good coupling, while not affecting the qubit characteristics.

The qubit charging energy obtained from the qubit spectroscopy (discussed later) is $E_C/h = 225 \pm 7$ MHz and according to $E_C = e^2/2C_\Sigma$ qubit capacitance is $C_\Sigma = 86 \pm 3$ fF. The SQUID consists of two Josephson junctions with maximal Josephson energy $E_{J0}/h = 15.7 \pm 0.5$ GHz. The energy of the qubit is controlled by a magnetic field of a surrounding solenoid, which tunes the effective Josephson energy E_J of the SQUID. The ratio $E_{J0}/E_C = 70$ defines the transmon regime and the ground-to-first excited state transition energy $E_{01} \approx \sqrt{8E_J E_C} - E_C$ [9].

The SAWs propagation speed at low temperatures in quartz is $v \approx 3.16$ km/s [24]. The periodicity of IDT stripes is $p = 980$ nm and that of the Bragg mirrors is $p/2$, which defines an optimal SAW wavelength and frequency: $\lambda = p$, $\omega_c/2\pi \approx 3.2$ GHz. Each element of our sample has a finite frequency bandwidth determined by its geometry. The calculated frequency characteristics of different elements are plotted in Fig. 2(a) and resulting bandwidth of the resonator is limited by the Bragg mirrors to about 33 MHz.

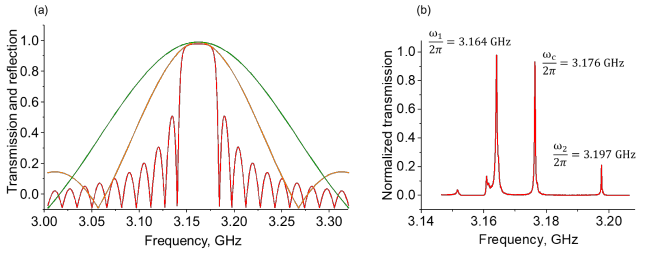

FIG. 2. Frequency characteristics (normalized to be 1 at maximum). (a) Calculated frequency characteristics of different circuit elements. The Bragg mirror reflectivity (red line), has the width of the main maximum $\Delta F_m = 33$ MHz. Green and yellow curves correspond to the simulated frequency dependence of the absolute values of transmission amplitudes for a signal, applied to the input IDT (yellow) or qubit IDT (green). The corresponding bandwidths are $\Delta F_{IDT} = 95$ MHz and $\Delta F_q = 143$ MHz. (b) Measured transmission through a SAW resonator. The central peak corresponds to the SAW mode, interacting with the qubit, since its IDT electrodes are located in acoustic field antinodes for this mode.

All measurements described below are performed in a dilution refrigerator at the base temperature of 20 mK. The thermal fluctuation energy is well below the energy of phonons, which is $\hbar\omega_c/k_B = 150$ mK (here k_B is the Boltzmann constant). To measure the acoustic response, we implement the same method and the mea-

surement circuit as the ones used in quantum optics experiments with the superconducting artificial atoms described for example in Refs. [22, 25]. The electromagnetic microwaves are transmitted from a vector network analyzer (VNA) through coaxial cables and then through an on-chip coplanar line to the input IDT port, where they are converted into SAWs in the resonator. The standing SAWs are converted into electromagnetic waves by the output IDT port. Then the signal is amplified by cryogenic amplifiers and measured by the VNA.

We first perform a measurement of a transmission amplitude through the resonator, which is shown in Fig. 2(b). In this measurement the qubit is away from the resonator resonance. We find three resonances with frequencies $\omega_1/2\pi = 3.164$ GHz, $\omega_c/2\pi = 3.176$ GHz and $\omega_2/2\pi = 3.197$ GHz. The full-width-at-half-maximum (FWHM) of square of transmission amplitude $|t|^2$ at ω_c is $\Delta\omega/2\pi = 0.332$ MHz. Taking into account that the frequency width is $\Delta\omega$ and the power applied to the resonator is P_{in} (from -134 to -128 dBm) we estimate the phonon number in the resonator to be in the range 10 – 40 ($N_{res} = P_{in}/\ \Delta\omega\hbar\omega_c$) in case of negligible internal loss. The phonon number can be even smaller, when the internal loss is not negligible compared to the external one.

Next, we demonstrate the interaction between the qubit and the SAW resonator in the quantum regime. We do that by monitoring the complex transmission amplitude t through the cavity at frequency ω_c as a function of magnetic field, applying a weak driving power to keep the effective phonon number in the resonator less than one. The transmission peak exhibits periodic anticrossings with the period corresponding to a flux quantum through the SQUID loop. The typical anticrossing is shown in Fig. 3. The anticrossing demonstrates the interaction of the two-level system with the SAW cavity and it disappears with an increase in the driving amplitude, as expected. Also, we make sure that there is indeed less than one phonon in the resonator by checking that the anti-crossing picture is not affected by the decrease of driving amplitude. Our estimate of the phonon number in the resonator at ω_c is much less than one, considering the applied power (ten times less compared to the first measurement shown in Fig. 2(b)) and the resonator linewidth broadening in the vicinity of the anticrossing..

To find an energy splitting of this anticrossing for the lowest excitation we use the following equation

$$E_{\pm} = \frac{\hbar(\omega_c + \omega_q) \pm \hbar\sqrt{(\omega_c - \omega_q)^2 + 4g^2}}{2} \qquad (2)$$

from diagonalization of the Hamiltonian of Eq. (1). Using this function, we acquire the coupling constant $g/2\pi = 15.7 \pm 0.2$ MHz from the fit of our anticrossing spectrum, as shown in Fig. 3(a, c). This means that total splitting is $2g/2\pi = 31.4$ MHz, which tightly fits in the bandwidth of the resonator $\Delta F_m = 33$ MHz. Note also that

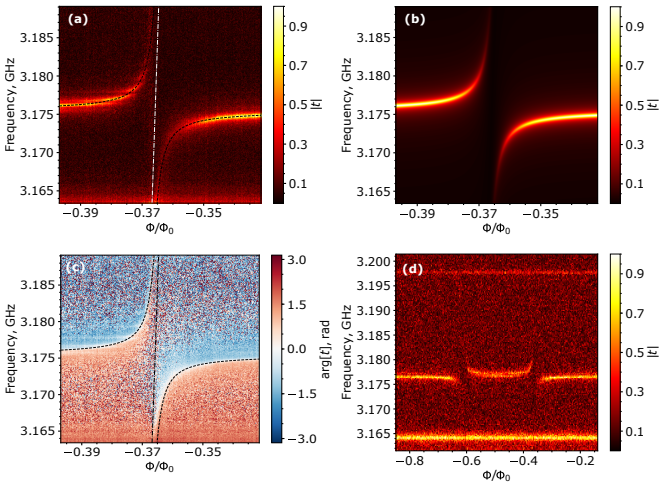

FIG. 3. Interaction of the qubit with the acoustic resonator. (a) and (c) panels represent amplitude ($|t|$) and phase ($\arg(t)$) of the transmission coefficient t through the SAW resonator in vicinity of the resonator frequency ω_c. The anticrossing demonstrates the interaction between the qubit and the resonator, when they are in resonance. The dashed line is the expected qubit energy without the interaction. The dotted line is the calculated energy splitting according to Eq. (2) with $g/2\pi = 15.7 \pm 0.2$ MHz. (b) The theretical plot of the transmission amplitude obtained from a master equation solving. (d) The transmission plot in wider frequency and magnetic field ranges, showing the splitting absence on the adjacent resonator modes.

the splitting does not occur at the adjacent resonator modes (see Fig. 3(d)). It means that these modes are only weakly coupled to the qubit, which signifies that maximums of amplitudes (antinodes) of the corresponding standing waves do not coincide with qubit electrode locations, as they do for the central mode.

In our next measurement we apply a method of dispersive readout known from the circuit QED [25] to characterize the qubit energies. By monitoring the transmission through the cavity at ω_c and sweeping the second probe tone ω_p we find a pattern with one well distinguished qubit resonance line, corresponding to the qubit transition energy E_{10} (Fig. 4). We also see a signature of a E_{12} transition as well as some higher order transitions. The pattern is periodic with the applied magnetic field and the period is expected to be the flux quantum Φ_0 through the SQUID. Measured qubit transition energies are in a good agreement with our expectations. Although the excitation of the qubit in the dispersive regime is performed through an acoustic resonator port, the excitation is electromagnetic in its nature. This is due to the fact that away from the acoustic resonance, the electromagnetic coupling is much stronger than the acoustic one, since the IDT ports have limited acoustic bandwidth of 95 MHz (see Fig. 2(a)). From our capacitance simulations, we find the effective qubit gate capacitance to be

$C_g \approx 0.1$ fF.

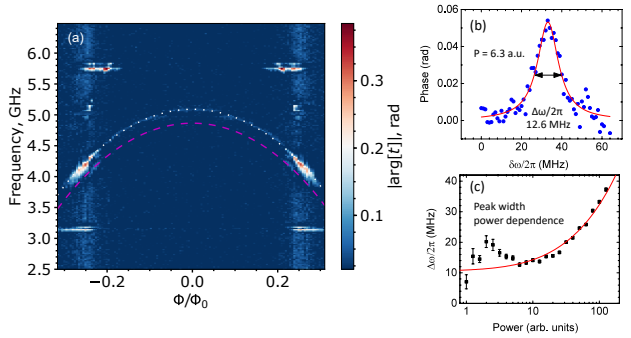

FIG. 4. (a)Two tone spectroscopy. The phase shift of the first tone signal transmission is shown by color. The vertical axis corresponds to the frequency sweep of the second tone. The horizontal axis corresponds to the magnetic flux through the SQUID. The dotted lines are the fitting curves, obtained from the qubit Hamiltonian (Eq. (1)) eigenstates calculation: E_{01} (white), E_{12} (magenta). The acoustic resonance is also seen at 3.176 GHz. There are also signatures of some other lines corresponding to higher order processes. From E_{01} fits we obtain qubit's charging energy $E_C = 0.21$ GHz and maximum Josephson energy $E_{J0} = 17.4$ GHz, which is in good agreement with our expectations. The first tone phase peak at the fixed magnetic flux $\Phi = 0.31\Phi_0$. (c) The peak width dependence on a driving power, fitted by $\delta\omega = \sqrt{\Gamma_1^2 + AP}$ (red curve).

We also extract the relaxation rate Γ_1 of the qubit (assuming there is no pure dephasing, which is usually valid for transmons) from an intrinsic width of the spectral line of the qubit by measuring it in the dispersive regime at $\Phi = 0.31$ and $\omega/2\pi = 3.85$ GHz – not far from the resonant point in the low driving limit. The typical peak is shown in Fig. 4(b) and the peak width dependence as a function of driving power is in Fig. 4(c). It is fitted by $\delta\omega = \sqrt{\Gamma_1^2 + AP}$, where P is the driving power and Γ_1 and A are the fitting parameters. Γ_1 is found to be 10.5 ± 1 MHz. We use that Γ_1 to solve the master equation and obtain the theoretical plot of the resonator transmission shown in Fig. 3(b), which is in good agreement to the experiment (Fig. 3(a)). The rather short lifetime can be a result of several different sources of dissipations: the dielectric; defects on the surface; dissipation in the thin and long qubit electrodes and some others.

Now we independently estimate the coupling g of the qubit to the resonator according to $\hbar g = \zeta e V_0$[2], where $\zeta = (E_J/2E_C)^{1/4} \approx 1.95$ at the anticrossing with $\Phi/\Phi_0 = 0.38$, e is the elementary charge and V_0 is the voltage, induced by zero-point fluctuations of the SAW mode. Power of the acoustic wave with amplitude ϕ_0 transferred in a width $W = 100$ μm is $P = \frac{\omega W \epsilon_\infty |\phi_0|^2}{2K^2}$ [27], where $\omega = 3.1$ GHz is the frequency of the wave, $\epsilon_\infty = 5 \times 10^{-11}$ F/m is the capacitance of a unit-aperture single-electrode transducer per period and $K^2 = 0.0012$ is a piezoelectric coupling constant. Energy of zero-point fluctuations in the acoustic resonator is: $E_{res} = 2PL_{eff}/v = \hbar\omega/2$, where $v = 3.16$ km/s is the SAW propagation speed and L_{eff} is the effective length of the resonator. This effective length consists of the distance between the resonator mirrors $L_0 = 110.7$ μm plus the penetration depth in these mirrors $L_p = p/(4|r_s|) = 17.5$ μm, where $|r_s| = 0.014$ is the absolute value of the reflection coefficient from one electrode [27]. Thus we obtain $L_{eff} = L_0 + 2L_p = 145.7$ μm. This allows us to get a value of the effective amplitude of the standing acoustic wave ϕ_0. We calculate the maximal possible induced voltage amplitude to be: $V_0 = 2\phi_0 = \sqrt{\frac{2\hbar v K^2}{L_{eff} W \epsilon_\infty}} = 3.3 \times 10^{-8}$ V, and $g_{max}/2\pi \approx 16$ MHz, which is close to the experimentally measured value. The actual value is also dependent on the stripe geometry.

Finally, in order to better understand the exact mechanism of our system excitation, we consider two driving terms in the full Hamiltonian: (i) the drive of the acoustic cavity via IDT: $H_{ac} = \hbar\Omega_{ac}(b^\dagger + b)\cos\omega t$ and (ii) the electric drive of the qubit: $H_{el} = \hbar\Omega_{el}(\sigma^+ + \sigma^-)\cos\omega t$, where Ω_{ac} and Ω_{el} are acoustic and electric driving amplitudes respectively. The acoustic driving amplitude at the resonance can be found as $\hbar\Omega_{ac} = \mu_{ac} V$, where $\mu_{ac} = C_{IDT} V_0 \approx C_\Sigma V_0 \approx 0.018$ e is the coupling between the voltage V applied to the input IDT and the resonator driving amplitude Ω_{ac}. The electric coupling between the IDT and the qubit can be expressed as $\hbar\Omega_{el} = \mu_{el} V$, where $\mu_{el} = C_g V_q$ and $V_q = 2e\zeta/C_\Sigma$ is the potential induced in the transmon qubit due to single Cooper pair transition. Substituting the numbers, we find $\mu_{el} = 2eC_g/C_\Sigma \approx 0.002e$. This means that at the resonance the electric coupling is weaker than the acoustic one ($\mu_{ac}/\mu_{el} \approx 9$).

In conclusion, we have experimentally demonstrated interaction between an artificial atom and a SAW resonator. The result is an important milestone for the future realization of quantum acoustics effects dual to quantum optics [28]. It can also be used to build compact devices for quantum informatics [29], since SAWs wavelength is smaller than electromagnetic by 5 orders of magnitude. Also SAW resonator can be designed to have multiple resonance modes, which can be utilized to place several qubits in one resonator and address them independently.

We would like to express our deep gratitude to Kirill Shulga and Nikolay Abramov for their contribution to the low temperature measurements. We also thank Aleksey Dmitriev and Alexander Korenkov for valuable discussions and their help in our experimental data analysis. We acknowledge Russian Science Foundation (grant N 16-12-00070) for supporting the work. This work was performed using technological equipment of MIPT

Shared Facilities Center and with financial support from the Ministry of Education and Science of the Russian Federation (Grant No. RFMEFI59417X0014).

* alexgood@list.ru
† oleg.astafiev@rhul.ac.uk

[1] A. D. O'Connell, M. Hofheinz, M. Ansmann, R. C. Bialczak, M. Lenander, E. Lucero, M. Neeley, D. Sank, M. Wang, D. Sank, H. Wang, M. Weides, J. M. Martinis, and A. N. Cleland, Nature **464**, 697 (2010).
[2] R. Manenti, A. F. Kockum, A. Patterson, T. Behrle, J. Rahamim, G. Tancredi, F. Nori, and P. J. Leek, Nature Communications **8**, 975 (2017).
[3] M. V. Gustafsson, T. Aref, A. F. Kockum, M. K. Ekström, G. Johansson, and P. Delsing, Science **346**, 207 (2014).
[4] M. LaHaye, J. Suh, P. Echternach, K. C. Schwab, and M. L. Roukes, Nature **459**, 960 (2009).
[5] J.-M. Pirkkalainen, S. Cho, J. Li, G. Paraoanu, P. Hakonen, and M. Sillanpää, Nature **494**, 211 (2013).
[6] F. Rouxinol, Y. Hao, F. Brito, A. Caldeira, E. Irish, and M. LaHaye, Nanotechnology **27**, 364003 (2016).
[7] Y. Nakamura, Y. A. Pashkin, and J. Tsai, nature **398**, 786 (1999).
[8] J. Mooij, T. Orlando, L. Levitov, L. Tian, C. H. Van der Wal, and S. Lloyd, Science **285**, 1036 (1999).
[9] J. Koch, M. Y. Terri, J. Gambetta, A. A. Houck, D. Schuster, J. Majer, A. Blais, M. H. Devoret, S. M. Girvin, and R. J. Schoelkopf, Physical Review A **76**, 042319 (2007).
[10] J. Sulkko, M. A. Sillanpaa, P. Hakkinen, L. Lechner, M. Helle, A. Fefferman, J. Parpia, and P. J. Hakonen, Nano letters **10**, 4884 (2010).
[11] C. Ockeloen-Korppi, E. Damskägg, J.-M. Pirkkalainen, T. Heikkilä, F. Massel, and M. Sillanpää, Physical Review Letters **118**, 103601 (2017).
[12] F. Massel, T. Heikkilä, J.-M. Pirkkalainen, S.-U. Cho, H. Saloniemi, P. J. Hakonen, and M. A. Sillanpää, Nature **480**, 351 (2011).
[13] T. Li, Y. A. Pashkin, O. Astafiev, Y. Nakamura, J. Tsai, and H. Im, Applied Physics Letters **92**, 043112 (2008).
[14] Y. Chu, P. Kharel, W. H. Renninger, L. D. Burkhart, L. Frunzio, P. T. Rakich, and R. J. Schoelkopf, Science **358**, 199 (2017).
[15] A. Noguchi, R. Yamazaki, Y. Tabuchi, and Y. Nakamura, Phys. Rev. Lett. **119**, 180505 (2017).
[16] V. S. Shumeiko, Phys. Rev. A **93**, 023838 (2016).
[17] D. P. A. Morgan, *Advances in Surface Acoustic Wave Technology, Systems and Applications*, 1st ed. (World Scientific, 2000) pp. 1–50.
[18] I. Court, IEEE Transactions on Microwave Theory and Techniques **17**, 968 (1969).
[19] R. Tancrell, M. Schulz, H. Barrett, L. Davis, and M. Holland, Proceedings of the IEEE **57**, 1211 (1969).
[20] P. Hartemann and E. Dieulesaint, Electron. Lett **5**, 657 (1969).
[21] T. E. Parker and G. K. Montress, IEEE transactions on ultrasonics, ferroelectrics, and frequency control **35**, 342 (1988).
[22] H. Wang, M. Hofheinz, M. Ansmann, R. Bialczak, E. Lucero, M. Neeley, A. O'connell, D. Sank, J. Wenner, and A. Cleland, Physical Review Letters **101**, 240401 (2008).
[23] O. Astafiev, A. M. Zagoskin, A. Abdumalikov, Y. A. Pashkin, T. Yamamoto, K. Inomata, Y. Nakamura, and J. Tsai, Science **327**, 840 (2010).
[24] T. Aref, P. Delsing, M. K. Ekström, A. F. Kockum, M. V. Gustafsson, G. Johansson, P. J. Leek, E. Magnusson, and R. Manenti, in *Superconducting Devices in Quantum Optics* (Springer, 2016) pp. 217–244.
[25] A. Wallraff, D. I. Schuster, A. Blais, L. Frunzio, R.-S. Huang, J. Majer, S. Kumar, S. M. Girvin, and R. J. Schoelkopf, Nature **431**, 162 (2004).
[26] R. Manenti, M. Peterer, A. Nersisyan, E. Magnusson, A. Patterson, and P. Leek, Physical Review B **93**, 041411 (2016).
[27] D. Morgan, *Surface acoustic wave filters: With applications to electronic communications and signal processing* (Academic Press, 2010).
[28] D. Rodrigues, J. Imbers, and A. Armour, Physical review letters **98**, 067204 (2007).
[29] A. F. Kockum, P. Delsing, and G. Johansson, Physical Review A **90**, 013837 (2014).